Ion Transport Control in Alkaline Water Electrolyzers at Elevated Temperatures Revealed by Molecular Simulations and Multiphysics Modeling

Anusha Tripathi, Viraj Bhatt, Shaswat Srivastava, Sanjeev Kumar, and Ananth Govind Rajan*

Department of Chemical Engineering, Indian Institute of Science, Bengaluru, 560012, Karnataka, India

(Received 10 October 2025; revised 29 May 2026; accepted 18 June 2026; published 30 July 2026)

Alkaline water electrolyzers (AWEs) offer a carbon dioxide-emission-free route to convert renewable electricity into hydrogen. Improving their efficiency requires a deep understanding of transport and kinetics within an electrolytic cell. By combining molecular simulations of ion diffusivities with detailed multiphysics simulations, we report here a surprising finding that neglecting the temperature dependence of ion transport in an AWE could lead to erroneous predictions of current density reducing with increasing temperature. This is because ion mobilities reduce with temperature, leading to severe transport limitations if diffusivities are considered to be independent of temperature. We model ion diffusion, migration, and convection via the Nernst-Planck formulation, fluid dynamics via the continuum Euler-Euler approach, along with electrode kinetics at the Butler-Volmer level of theory. We carry out molecular dynamics simulations to determine the temperature dependence of OH^- and K^+ diffusivities and show that considering temperature-dependent diffusivities leads to the current density increasing with temperature. We also demonstrate that gas bubble formation and OH^- concentration gradients lead to reduced electrolyte conductivity near the electrodes. The higher levels of cathodic gas production, as compared to those at the anode, lead to asymmetries in the concentration profiles. We provide physical understanding regarding these observations, including that at high cell potentials, transport limitations play a crucial role in modulating AWE performance. Overall, our findings provide critical insights into the interplay between ion transport, temperature, and electrochemical performance, which are crucial for accurate multiscale simulations and modeling-based optimization of such devices.

DOI: 10.1103/8zs3-7ynk

I. INTRODUCTION

To meet net-zero emission targets, the traditional methods of hydrogen (H_2) generation, such as coal gasification and hydrocarbon reforming, need to be replaced by suitable carbon dioxide (CO_2)-emission-free methods. Electrocatalytic water splitting using energy from renewable resources like solar and wind caters to this shift toward green H_2 production [1]. Currently, three electrolysis technologies exist, which differ from each other in their operating mechanism, electrode material, type of ion-exchange membrane (or separator) used, electrolyte solution, charge-carrier species involved, and operating conditions [2–6]. These are alkaline water electrolyzers (AWEs), proton exchange membrane electrolyzers, and solid-oxide electrolyzers. Of these, AWEs have emerged as a commercially viable option, owing to their working mechanism, which does not require noble metals as electrodes or an expensive ion-exchange membrane. Nevertheless, a detailed understanding of the coupled mass/charge transport and reaction kinetics inside AWEs is presently lacking, preventing the optimization of operating conditions to achieve optimal performance.

From the point of view of industrial relevance, the benchmark current density for an electrolyzer is >500 mA cm^{-2} at an overall overpotential <400 mV, with operating temperatures around 80–90 °C [5,6]. With an applied voltage in the range of 1.7–2.0 V, AWEs offer a moderate efficiency of 60%–80%, though a current density of up to 600 mA cm^{-2} is now realized in lab-scale units [7]. To compete with traditional H_2 production methods, improvements in the output efficiency and hydrogen generation rates of AWEs are essential, which necessitate going to elevated temperatures, although still below the boiling point of water [8]. Understanding the working of electrolyzers under such conditions is thus necessary to reduce key resistances, including charge-transfer energy barriers and mass-transport resistances in the electrolyte and the separator. With respect to electrode materials, several electrocatalysts that can offer high activity with acceptable longevity are being explored to minimize

*Contact author: ananthgr@iisc.ac.in

charge-transfer losses (i.e., the activation overpotential) [9–15]. Independent of these materials, all of these resistances need to be analyzed under realistic operating conditions, while considering two fluid phases in the electrolyte solution. This has been addressed for some electrochemical systems dealing with two-phase electrolytes, such as fuel cells [16], CO_2 electrolyzers [17], zinc-air batteries [18], etc. In this work, we enable a temperature-dependent quantification of these multiphysical aspects of AWEs, which opens up avenues for optimizing operating conditions and other physical parameters. Our analysis reveals ion transport as a critical factor in elevated-temperature operation.

To link the overall electrolyzer performance with various important factors, numerous empirical, semiempirical, and physics-based models have been proposed in the past [19,20]. Of these models, the empirical model proposed by Ulleberg [21] is widely used. It provides a correlation for the stack voltage as a function of the applied current and operating temperature. This work was further expanded to capture experimental trends with higher sensitivity through additional parameters such as electrode discharge [22,23], operating pressure [22,23], and half-cell width [22]. Another study showed that more accurate predictions were possible by including empirical expressions for activation and Ohmic overpotentials [24]. An approach assuming a well-mixed electrolyte and a correlation for electrolyte conductivity has also been implemented to predict the current density for a variety of operational parameters, such as the separator porosity and thickness, its distance from electrodes, and the operating temperature [25,26].

To elucidate the effects of the presence of gas bubbles in the electrolyte, two-phase fluid flow models have been used. The Euler-Euler laminar flow [27], Euler-Euler turbulent flow [28], and Euler-Lagrange flow [29] formulations have been adapted to resolve the two fluid phases. The Euler-Euler model solves for both the liquid electrolyte and the gas bubble flow in a homogeneous manner, while the Euler-Lagrange approach resolves the gas bubbles by individually tracking them [30]. A comprehensive model, such as the one proposed by Mat *et al.* [31] solves for the void distribution, velocity profiles, and the impact of bubble accumulation on the current density distribution through transport equations, electrochemical species balance, and buoyancy effects. Lately, machine learning-coupled fluid dynamics models have also been proposed to solve for and optimize the working of AWEs. Babay *et al.* [32] accounted for porous electrodes and the effect of variation in the concentration of the electrolyte solution, operating temperature, and physical features like the separator porosity and gas bubble diameter, using artificial neural networks (ANNs). Similarly, based on ANNs, the model by Sirat *et al.* [33] predicts effects of changes in the operating temperature, electrolyte concentration, and electrode-diaphragm width.

However, in these previous studies, a unified transport description addressing the effect of temperature on the overall performance of AWEs is not available. Often, the quantitative details of losses due to the transport of ions across the cell gap are subsumed in a correlation for electrolyte conductivity, or the effect of temperature on transport and kinetics is not addressed. A comprehensive study, establishing a relationship between the operating temperature and the performance of AWEs, requires a coupled understanding of hydrodynamics, ionic transport, and electrochemical reactions. This entails solving for both liquid and gas phases in the electrolyte, along with active transport modes at the bulk and molecular length scales. To address this gap, we present a framework that is targeted to stand as an overarching mathematical model, providing complete understanding of the working of AWEs pertaining to (i) the effect of operating temperature, (ii) the role of molecular-scale transport processes (diffusion and migration), (iii) the presence of two fluid phases in the electrolyte, and (iv) the nonuniformity in the gas generation rates and current distribution along the flow direction. To capture the effect of the operating temperature on the ionic transport rates, we use molecular dynamics (MD) simulations to determine the temperature-dependent diffusion coefficients of OH^- and K^+ ions. Furthermore, we use the Nernst-Planck formulation [34] coupled with the Euler-Euler laminar flow model [30,35] to account for mass and momentum conservation. Thereby, the proposed model addresses the multiphysical aspects of water electrolyzers in a comprehensive, multiscale manner.

II. MODEL DEVELOPMENT

AWEs involve complicated fluid-dynamical behavior of the gas-dispersed liquid phase, mass transport of ionic species across the interelectrode region, and electrochemical reactions at the electrodes. The water molecules decompose at the cathode into H_2 and OH^- ions. The hydroxide ions carry the current across the cell through the electrolyte solution and the separator and get oxidized at the anode, liberating oxygen (O_2) gas. The alkalinity of the electrolyte ensures an abundance of OH^- ions, thereby increasing the conductivity of pure water. The dissolved gas molecules nucleate to form gas bubbles, which, under their own buoyancy and the influence of the electrolyte flow, exit their respective half-cells. A schematic depicting the operation of an AWE is presented in Fig. 1 (left). As per the chosen coordinates, gravity acts in the negative y direction. The equations for the involved redox reactions are as follows:

$$\text{Anode}: 4OH^- \rightarrow O_2 + 2H_2O + 4e^- \quad (1)$$

$$\text{Cathode}: 4H_2O + 4e^- \rightarrow 2H_2 + 4OH^- \quad (2)$$

$$\text{Overall}: 2H_2O \rightarrow 2H_2 + O_2 \quad (3)$$

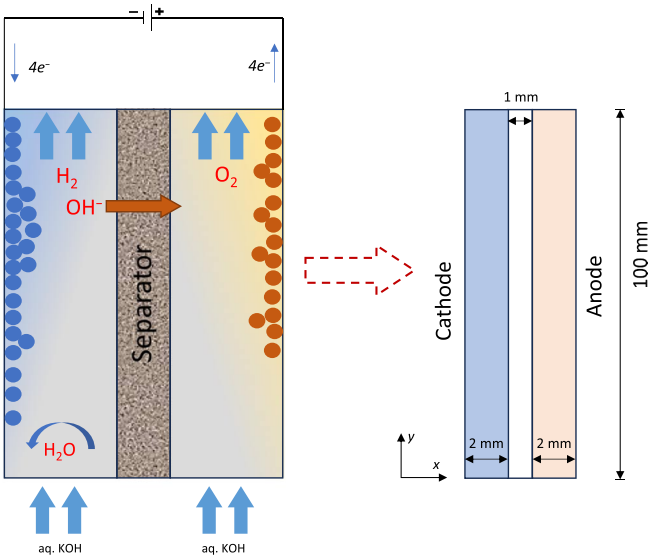

FIG. 1. Schematic of an alkaline water electrolyzer (left) along with the simplified model geometry used in the simulations in this work (right).

where the oxygen evolution reaction (OER) occurs at the anode and the hydrogen evolution reaction (HER) occurs at the cathode.

A. Geometry and model assumptions

The geometry of the AWE simulated in this work is presented in Fig. 1 (right). The cell configuration investigated in the present work has electrodes mounted in vertical planes, flush with the side walls. The two compartments, each of width 2 mm, constitute the two half-cells. These are divided by a 1-mm-thick separator. The detailed dimensions of the system are provided in Table I. The following assumptions have been made while solving the model equations of the AWE: [25,32,36,37]

(1) A two-dimensional formulation, which has been extensively used to model several other electrochemical systems involving the flow of electrolyte and electrochemical reactions [36,38], has been adapted to represent the AWE.
(2) The gas-dispersed liquid phase is considered fully laminar and incompressible. The two phases share the same pressure field.
(3) A constant bubble size (50 μm) is assumed throughout the domain. Bubble growth, coalescence, and breakup mechanisms are neglected. Notably, in a concentrated alkaline electrolyte, bubbles detach predominantly as individual entities with minimal coalescence [1], leading to nearly constant bubble sizes everywhere. See Supplemental Material for a more detailed justification [39].
(4) The distribution of dissolved gases in the electrolyte solution and bubble dynamics are not considered, except for accounting for the surface coverage by bubbles in electrochemical kinetics.
(5) Isothermal conditions are assumed everywhere in the cell, along with no reaction in the bulk electrolyte. A previous study showed that the temperature difference across the cell remains on the order of a few kelvin under higher current densities (> 2000 A/m^2) [41]. For our model predictions (see below), with an average current density of less than 1100 A/m^2 and a high flow rate of electrolyte, the assumption of isothermal operation is reasonable. See Supplemental Material for a detailed justification [39].
(6) The solid electrodes are nonporous and highly conductive, leading to negligible potential gradients; hence, only the electrolyte and separator are modeled as a two-phase domain.
(7) We ignore the electrical double layers at the electrode-electrolyte interfaces in this study, given the extremely small equilibration timescales.

TABLE I. Parameters used for the simulation of the AWE considered.

Parameters	Value	Unit	Parameters	Value	Unit
p_{ref}	1	atm	z_{K^+}	1	
F	96485	C/mol	z_{OH^-}	−1	
R	8.314	J/mol/K	Number of electrons	4	
$E^0_{\text{eq,ref},+}$	Table II	V	$E^0_{\text{eq,ref},-}$	Table II	V
c_{ref}	1	M	Bubble diameter (d_b)	50	μm
H_2 bubble dispersion factor [32]	5	m/s	O_2 bubble dispersion factor [32]	10	m/s
$j_{0,-}$ [51]	10	A/m^2	$j_{0,+}$ [51]	1×10^{-4}	A/m^2
$\alpha_{a,\text{HER}}$ [51]	1		$\alpha_{c,\text{HER}}$ [51]	1	
$\alpha_{a,\text{OER}}$ [51]	1.7		$\alpha_{c,\text{OER}}$ [51]	0.1	
H_2 compartment width (W_{H_2})	2	mm	O_2 compartment width (W_{O_2})	2	mm
Separator width (W_{sep})	1	mm	Electrode height (H_{elec})	100	mm
Separator porosity [52]	0.3		Gas pressure	1	atm
Inlet electrolyte concentration	1000	mol/m^3	Average inlet velocity, cathode and anode	1	m/s

B. Euler-Euler laminar flow model

The Euler-Euler laminar flow model [42] is a widely implemented simulation approach [22,27,28] as it captures the essential features of gas-liquid flow at reasonable computational costs [1]. It accounts for the volume fraction of each phase—the dispersed phase (gas bubbles, in our case) and the continuous phase (liquid electrolyte, in our case)—without actually tracking the interfaces (locations and sizes) of the generated gas bubbles. Both phases are considered continuous and interpenetrating. This dual-phase consideration is crucial for accurately calculating the local interplay between the gas and liquid phases.

The continuity equation for the dispersed-continuous phase mixture and the rate of change of the gas phase volume fraction (ϕ_d), respectively, are

$$\nabla \cdot (\phi_d \mathbf{u}_d + \phi_c \mathbf{u}_c) = m_{dc}\left(\frac{1}{\rho_c} - \frac{1}{\rho_d}\right) \tag{4}$$

$$\frac{\partial \phi_d}{\partial t} + \nabla \cdot (\phi_d \mathbf{u}_d) = -\frac{m_{dc}}{\rho_d}, \tag{5}$$

where ρ_c and ρ_d denote the continuous and the dispersed phase density, respectively, and $\mathbf{u}_c$ and $\mathbf{u}_d$ are the continuous and dispersed phase velocities, respectively. Further, m_{dc} is the interphase mass transfer rate from the dispersed to the continuous phase per unit volume. We set it to zero, such that the two fluid phases transfer momentum, but their masses are individually conserved. The continuous and dispersed phase volume fractions are related as $\phi_c = 1 - \phi_d \cdot \phi_d$ changes with time, until a steady state is reached, in response to gas generation through the equation below, defined at the electrodes

$$\phi_d \mathbf{u}_d \cdot \mathbf{n} = \frac{\dot{m}_g''}{\rho_d}, \tag{6}$$

where $\dot{m}_g''$ is the mass flux of the gas produced at an electrode and $\mathbf{n}$ denotes the unit normal vector to the electrode. The former quantity is expressed in terms of the local current density j_s at the electrode (which depends on the position y along the electrode), the molar mass of the gas M_g, and the number of electrons transferred per molecule of gas n_e, as

$$\dot{m}_g'' = \frac{j_{s,\pm} M_g}{n_e F}, \tag{7}$$

where F is the Faraday constant. Further, $+$ refers to the anode and $-$ refers to the cathode. Therefore, for each electrode, we get:

(i) Hydrogen electrode (HER):

$$\dot{m}_{\mathrm{H_2}}'' = \frac{j_{s,-} M_{\mathrm{H_2}}}{2F}. \tag{8}$$

(ii) Oxygen electrode (OER):

$$\dot{m}_{\mathrm{O_2}}'' = \frac{j_{s,+} M_{\mathrm{O_2}}}{4F}. \tag{9}$$

The momentum balance for the continuous electrolyte phase is given as

$$\rho_c \phi_c \left[\frac{\partial \mathbf{u}_c}{\partial t} + \mathbf{u}_c \nabla \cdot \mathbf{u}_c\right] = -\phi_c \nabla p + \phi_c \nabla \cdot \boldsymbol{\tau}_c + \phi_c \rho_c \mathbf{g} + \mathbf{F}_{m,c} + \phi_c \mathbf{F}_c + m_{dc}(\mathbf{u}_{\mathrm{slip}} - \mathbf{u}_c), \tag{10}$$

where p is the two-phase mixture pressure, $\boldsymbol{\tau}_c$ is the viscous stress tensor in the continuous phase, $\mathbf{g}$ is the gravitational acceleration, $\mathbf{F}_{m,c}$ denotes the interphase momentum transfer rate per unit volume for the continuous phase, $\mathbf{F}_c$ denotes the volume force term, and $\mathbf{u}_{\mathrm{slip}}$ is the slip velocity at the interface given as

$$u_{\mathrm{slip}} = \sqrt{(u_{d,x} - u_{c,x})^2 + (u_{d,y} - u_{c,y})^2}$$

where $u_{d,x}$ and $u_{d,y}$ represent the dispersed phase velocity components in the x and y directions, respectively. Similarly, $u_{c,x}$ and $u_{c,y}$ denote the continuous phase velocity components in the x and y directions, respectively.

Next, the momentum balance for the dispersed gas phase is given as

$$\rho_d \phi_d \left[\frac{\partial \mathbf{u}_d}{\partial t} + \mathbf{u}_d \nabla \cdot \mathbf{u}_d\right] = -\phi_d \nabla p + \phi_d \nabla \cdot \boldsymbol{\tau}_d + \phi_d \rho_d \mathbf{g} + \mathbf{F}_{m,d} + \phi_d \mathbf{F}_d + m_{dc}(\mathbf{u}_{\mathrm{slip}} - \mathbf{u}_d), \tag{11}$$

where $\boldsymbol{\tau}_d$ is the viscous stress tensor in the dispersed phase and $\mathbf{F}_{m,d}$ denotes the rate of interphase momentum transfer per unit volume.

The interphase momentum transfer is due to the drag forces between the buoyant gas bubbles and the surrounding liquid. Its rate per unit volume is calculated as

$$\mathbf{F}_{m,c} = -\mathbf{F}_{m,d} = \frac{3}{4} C_d \frac{\phi_d \rho_c}{d_b} |\mathbf{u}_d - \mathbf{u}_c|(\mathbf{u}_d - \mathbf{u}_c), \quad (12)$$

where C_d represents the drag coefficient. C_d is estimated through correlations, which in turn depend on the bubble-size distribution and the Reynolds number (Re). Re is defined based on the bubble diameter (d_b), which in this study is assumed to be monodisperse, with a value of 50 μm [27,43]. We used the *Schiller-Naumann* slip model to estimate C_d as it is applicable for small, spherical bubbles (< 1 mm) and Reynolds numbers up to 2.5×10^3 [44–46], defined as

$$C_d = \begin{cases} \frac{24}{\mathrm{Re}}(1 + 0.15\mathrm{Re}^{0.687}), & \text{if } \mathrm{Re} \le 1000. \\ 0.44, & \text{if } \mathrm{Re} > 1000. \end{cases} \quad (13)$$

The volume force (on a volumetric basis) is accounted for using the bubble-dispersion model [32,42].

$$\mathbf{F}_c = -\mathbf{F}_d = \phi_d \rho_c \frac{K_g}{d_b} |\mathbf{u}_d - \mathbf{u}_c| \nabla \phi_d, \quad (14)$$

where K_g/d_b is the gas bubble dispersion factor, defined individually for both the half-cells (see Table I).

C. Current distribution in the electrolyte

The current distribution model equations account for the effect of the electrolyte composition and resistances on the electrochemical process by solving the Nernst-Planck equation for each chemical species, describing their transport through diffusion, migration, and convection, along with electrode kinetics [47]. Thus, at the electrode-electrolyte interface, the current density of charge-transfer reactions is determined by both the overpotential and the concentration of the participating ionic species at the interface.

The balance equations for the concentrations c_i of the ionic species are as follows:

$$\frac{\partial(\phi_c c_i)}{\partial t} + \nabla \cdot \mathbf{N}_i = \phi_c R_i \qquad i = \mathrm{OH^-},\ \mathrm{K^+}, \quad (15)$$

where $\mathbf{N}_i$ is the flux of the species in the electrolyte solution and R_i denotes a bulk-volume source/sink reaction term. For our system, the R_i term is zero. The flux $\mathbf{N}_i$ is given by the Nernst-Planck equation as

$$\mathbf{N}_i = -D_{i,\mathrm{eff}} \nabla c_i - z_i c_i u_{i,\mathrm{eff}} F \nabla \varphi_l + c_i \mathbf{u} \quad (16)$$

where $D_{i,\mathrm{eff}}$ is the effective diffusivity and can be evaluated from the Bruggeman correlation [48] as $D_{i,\mathrm{eff}} = \phi_c^{1.5} D_i$, z_i is the valency of species i, $u_{i,\mathrm{eff}}$ is the ionic mobility ($= D_{i,\mathrm{eff}}/\mathrm{RT}$), and φ_l is the potential field in the electrolyte (liquid). F, R, and T are Faraday's constant, gas constant, and absolute temperature, respectively. $\mathbf{u}$ is the local electrolyte velocity that comes from solving the Euler-Euler flow equations. The three terms, as given in the order on the right-hand side of the equation, represent the diffusive, migrational, and convective fluxes for the individual species.

The current distribution model has three unknown variables. These are the concentrations of the ionic species ($\mathrm{OH^-}, \mathrm{K^+}$) and the electric potential (φ). The spatial variation of potential is typically defined using the Poisson equation as

$$\nabla^2 \varphi = -\frac{F}{\epsilon} \sum_i z_i c_i, \quad (17)$$

where ϵ denotes the permittivity of the medium.

The complete set of these three equations, therefore, gives a closed system of equations. However, the solution using the Poisson equation is computationally expensive. This is because the term F/ϵ [Eq. (17)] is a constant of very large magnitude (1.4×10^{16} V · cm) which admits extremely small values of $\sum_i z_i c_i$. Alternatively, Newman and Balsara [47] argue that for most systems, the Poisson equation could be replaced with the electroneutrality condition [Eq. (18)]. Indeed, significant charge separation generally requires very large electric field strengths. The electric field magnitude in the present system is estimated to be 360 V/m, which is several orders of magnitude smaller than the fields typically associated with substantial space-charge formation in electrochemical double layers [47]. This allows the system of equations to be closed without the Poisson equation. We thus solve the model by imposing the electroneutrality condition.

$$\sum_i z_i c_i = 0 \quad (18)$$

The current in the electrolyte solution, $\mathbf{j}_l$, is due to the motion of the charged species. Hence, the current density at any point can be evaluated as $\mathbf{j}_l = F \sum z_i \mathbf{N}_i$. The electroneutrality condition applied over the summed fluxes from Eq. (16) for all ionic species reduces the contribution of convective flow to the electrical current to zero. Hence, we get

$$\mathbf{j}_l = F \sum_i z_i (-D_i \nabla c_i - z_i c_i u_{i,\mathrm{eff}} F \nabla \varphi_l), \quad (19)$$

where the two terms on the right-hand side represent the diffusion and electromigration contributions to the ionic

current, respectively. The electroneutrality condition ensures conservation of charge in the electrolyte, making the divergence of current density exactly zero.

In regions wherein ∇c becomes zero, the total ionic current is sustained by the electromigration of ions alone. With the electrolyte conductivity defined as $\kappa = F^2 \sum_i z_i^2 c_i u_{i,\text{eff}}$ [47], the above equation then simply reduces to an expression of Ohm's law as

$$\mathbf{j}_{\text{migration}} = -\kappa \nabla \varphi_l. \tag{20}$$

The transport equations for the active species [Eq. (15)] along with the electroneutrality condition are also solved for the separator [Eq. (18)], equivalently, as an interpenetrating homogenized solid-liquid phase with a volume fraction (ϵ_{sep}) defined for the porosity of the separator. The diffusivity of the ionic species is thus also corrected through Bruggeman's relation, $D_{i,\text{eff}} = \epsilon_{\text{sep}}^{1.5} D_i$. This description is valid when the dispersed gases in both half-cells do not reach the separator interfaces in the way that all the gas liberated at the electrodes is swept out of the electrolyzer under the prevailing flow field.

1. Temperature dependence of the reference equilibrium Nernst potential

The reversible cell voltage was calculated using the Nernst equation [Eq. (21)], for both electrodes as

$$E_{\text{eq},\pm} = E^0_{\text{eq,ref},\pm}(T) - \frac{RT}{nF} \ln \left(\frac{c_{\text{OH}^-}}{c_{\text{ref}}} \right)^{\nu_{\text{OH}^-}} \tag{21}$$

where c_{ref} is the reference concentration for the active species, i.e., OH^-, taken equal to 1 M, and ν_{OH^-} is the stoichiometric coefficient for OH^-, i.e., -4 for the OER (at the anode) and 4 for the HER (at the cathode). The reference equilibrium potential $E^0_{\text{eq,ref},\pm}(T)$ is a function of the operating temperature and is the minimum potential required for the electrochemical reactions to proceed at the electrodes under equilibrium conditions.

We have extracted the values of these potentials from an inbuilt function of the AWE module available in COMSOL Multiphysics [49], which are tabulated in Table II in columns 2 and 3. We validate these values using an empirical relation from the literature [8,50]:

$$E^0_{\text{eq,ref}}(T) = 1.5184 - 1.54 \times 10^{-3} T + 9.523 \times 10^{-5} T \log T + 9.84 \times 10^{-8} T^2 \tag{22}$$

The relation above is a single-valued output function under the assumption that the HER electrode remains at zero potential during the process, and the total equilibrium potential is attributed to the OER electrode. In column 4, we report $E_{\text{eq,cell}} = E_{\text{eq,OER}} - E_{\text{eq,HER}}$. We note a good agreement between the COMSOL in-built function and the correlation obtained from the literature, thus validating the temperature-dependent thermodynamics employed in this work.

2. Nonuniformity in the current distribution

The bottom-to-top flow of the electrolyte solution involves flow direction-dependent concentration profiles on account of developing boundary layers. Therefore, the transport resistances on the electrolyte side vary downstream, resulting in a nonuniformity in the current density distribution. On the other hand, the electrode potential remains uniform throughout on account of high electrode conductivity. The predicted average current density j, therefore, relates to the distributed current density, $j_{s,\pm}$ (over the electrode length H_{elec}) as

$$j = \frac{1}{H_{\text{elec}}} \int_0^{H_{\text{elec}}} j_{s,\pm} \, \text{dy} \tag{23}$$

3. Kinetics of the electrochemical reactions involved

Along with solving the transport model for the ionic species to account for their movement in the electrolyte domain, it is also essential to account for the influence of the availability of the participating ionic species on the kinetics. The Butler-Volmer equation [47] relates the electrode kinetics with the activation overpotential and the concentration of the reduced and oxidized species at the electrode/electrolyte interface, as defined below for the anode and the cathode:

TABLE II. Equilibrium potential for the HER and OER at various temperatures.

	COMSOL predictions, current work [49]			Correlation predictions [50]
Temperature (°C)	$E_{\text{eq,HER}}$	$E_{\text{eq,OER}}$	$E_{\text{eq,OER}} - E_{\text{eq,HER}}$	$E_{\text{eq,cell}}$
25	−0.0887	1.1409	1.229	1.229
40	−0.089	1.1271	1.21	1.21
60	−0.088	1.107	1.19	1.2
80	−0.085	1.085	1.17	1.18

$$j_{s,+} = j_{0,\mathrm{eff},+}\left(\frac{c_{\mathrm{OH}^-}}{c_{\mathrm{ref}}}\exp\left(\frac{\alpha_{a,\mathrm{OER}}F\eta_+}{RT}\right) - \exp\left(\frac{-\alpha_{c,\mathrm{OER}}F\eta_+}{RT}\right)\right) \tag{24}$$

$$j_{s,-} = j_{0,\mathrm{eff},-}\left(\exp\left(-\frac{\alpha_{c,\mathrm{HER}}F\eta_-}{RT}\right) - \frac{c_{\mathrm{OH}^-}}{c_{\mathrm{ref}}}\exp\left(\frac{\alpha_{a,\mathrm{HER}}F\eta_-}{RT}\right)\right), \tag{25}$$

where $j_{0,\mathrm{eff},\pm}$ is the effective exchange current density and is defined uniquely for both electrodes, and T denotes the absolute system temperature. The occlusion of the reactive electrode surface due to the presence of the bubbles on the interface (without accounting for any adherence of bubbles on the surface) is corrected by multiplying the electrolyte (liquid phase) volume fraction close to the electrode interface by the intrinsic exchange current density, $j_{0,\pm}$ (see Table I). Hence, $j_{0,\mathrm{eff},\pm} = j_{0,\pm}\phi_c(x_\pm, y)$, where $x_+ = 0$ and $x_- = W_{\mathrm{cell}}$ represent the cathode and anode, respectively. $\alpha_{a,\mathrm{OER}}$ and $\alpha_{c,\mathrm{OER}}$ are the anodic and cathodic charge-transfer coefficients for the OER, respectively, $\alpha_{a,\mathrm{HER}}$ and $\alpha_{c,\mathrm{HER}}$ are the anodic and cathodic charge-transfer coefficients for the HER, respectively (see Table I), and η_+ and η_- are the activation overpotentials for the anodic and cathodic reactions, respectively.

The activation overpotentials for the anodic and cathodic Butler-Volmer expressions are defined using Eq. (26):

$$\eta_\pm = (\varphi_{\mathrm{s,ext},\pm} - \varphi_{l,\pm}) - E^0_{\mathrm{eq,\ ref},\pm}, \tag{26}$$

where $\varphi_{l,\pm}$ is the electrolyte potential right beside the electrode, which is obtained from the Nernst-Planck equation. Further, the overall cell potential, E, which is imposed on the system for a constant potential operation, is defined using Eq. (27):

$$E = \varphi_{\mathrm{s,ext},+} - \varphi_{\mathrm{s,ext},-}. \tag{27}$$

The parameters for the Butler-Volmer equations and Nernst potential equations are provided in Table I.

4. Boundary conditions

The boundary conditions at the *inlet* and the *outlet* for current distribution and *Euler-Euler* laminar flow models are recorded in Table III. The electrolyte solution enters the two half-cells with a fully developed parabolic profile at $y = 0$, with the mean velocity, v_{in} equal to 1 m/s. At the electrodes and separator surfaces, the *no-slip* boundary condition was imposed for the fluid flow. The cathode is grounded, and the specified external potential is applied to the anode, i.e.,

$$\phi_{\mathrm{s,ext},-} = 0\ \mathrm{V} \tag{28}$$

$$\phi_{\mathrm{s,ext},+} = E. \tag{29}$$

TABLE III. Inlet and outlet boundary conditions.

	Current distribution	Laminar flow
At the inlet	$\mathbf{j}\cdot\mathbf{y} = 0$ $c_0 = c_{\mathrm{KOH}}$	$u_{cx}(x,0,t) = 0$ $u_{cy}(x,0,t) = v_{\mathrm{in}}$ $u_{dx}(x,0,t) = 0$ $u_{dy}(x,0,t) = v_{\mathrm{in}}$ $\phi_d(x,0,t)\mathbf{u}_d(x,0,t)\cdot\mathbf{y} = 0$
At the outlet	$\mathbf{j}\cdot\mathbf{y} = 0$ $-D_i\nabla c_i\cdot\mathbf{y} = 0$	$p(x, H_{\mathrm{elec}}) = 0$

5. Computational details

The model equations with appropriate boundary and initial conditions were solved using the COMSOL Multiphysics package, version 5.6a, based on the finite element discretization method. An initialization study was executed first without considering the presence of the gas phase in the electrolyte (ϕ_d set to zero) to arrive at a set of informed initial values for the physical quantities like velocity, pressure, concentration, and temperature. These values were then fed to a time-dependent solver and then solved by considering the mass flux of gases into the electrolyte. All the results presented in the current work correspond to the time when these time-dependent simulations reached a steady state.

To precisely incorporate the sharp gradients in the concentration of species and gas phase volume fraction (near the electrodes and separator) and simultaneously minimize the computational time, a mapped mesh approach was adapted. To assess the mesh dependence, we carried out studies using four different discretization levels of mesh: (a) coarse, (b) fine, (c) finer, and (d) extra fine, containing 27 500, 29 500, 32 500, and 34 500 elements, respectively. The average current density differed by only 0.17%, and the corresponding concentration, potential, and volume-fraction profiles were indistinguishable between (c) and (d). We, therefore, chose the finer mesh (c) for all simulations. A tolerance of 10^{-4} was specified on the numerical solution. The schematic of the 2D cell geometry used in the simulations was provided earlier in Fig. 1. The values of all the physical parameters and the cell geometry used in this study are provided in Table I.

D. Molecular dynamics simulations for estimating temperature dependence of ionic diffusivities

The Large-scale Atomic/Molecular Massively Parallel Simulator (LAMMPS) package [53] was used to conduct the MD simulations. The PACKMOL code [54] was used to

generate the electrolyte configuration based on the electrolyte concentration. The final LAMMPS input files were generated using the fftool code. The water molecules were modeled using the TIP4P/2005 model [55]. Potassium hydroxide was modeled as dissociated ions, i.e., potassium and hydroxide ions, using the modified Madrid transport force field [56]. The bonds and angles within the water molecules were constrained using the SHAKE algorithm [57]. The hydroxide ion bond was also constrained using the same algorithm. Lorentz-Berthelot mixing rules were employed for all ion-ion and ion-water self and cross interactions, except for the $KOH - H_2O$ Lennard-Jones interactions, for which the specific parameters are adapted from Habibi *et al.* [56]. The distance cutoffs for the Lennard-Jones (LJ) and the short-range Columbic interactions were set to 10 and 12 Å, respectively. At the same time, long-range interactions were also considered for the Coulombic forces using the particle-particle-particle mesh method [58] with an accuracy of 10^{-5} for the per-atom force in the long-range solver. The time step for the simulations was kept at 1 fs and simulations were conducted in the isothermal-isobaric ensemble. All simulations were first equilibrated with a 1-ns run, and then a production run of 10 ns was carried out. The system's temperature was maintained using the Nosé-Hoover thermostat [59,60] to be a specific value in the range 298.15–353.15 K. The system's pressure was maintained at 1 atmosphere in all simulations using the Nosé-Hoover barostat [61]. The concentration of the KOH solution was kept at 1 molal. Based on that, the system consisted of 5000 water molecules and 90 units each of potassium and hydroxide ions. To obtain the diffusivity values more accurately, five nonidentical configurations with distinct initial molecular geometry and distinct seed values for the initial velocity generation were considered to initialize the MD simulations.

The diffusion coefficient of any species can be computed using the mean squared displacement (MSD) of that particular species. Using the MD simulations, MSD was obtained for the OH^- and K^+ ions from five independent runs with random initial atomic positions and velocities (see Supplemental Material [39]). The MSD is given as

$$M_i(\tau) = \langle |\mathbf{r}_i(\tau) - \mathbf{r}_i(0)|^2 \rangle \tag{30}$$

where $M_i(\tau)$ represents the MSD of the species i, $\mathbf{r}_i(t)$ denotes the position of particle i at time t, and τ represents the sampling frequency for the MSD calculations. After the estimation of $M_i(\tau)$, the diffusivity of the species can be estimated using Einstein's relation [34], given as

$$D_i'(\tau) = \frac{M_i(\tau)}{2\alpha\tau} \tag{31}$$

where D_i' represents the diffusivity of the species i without considering finite-size effects and α is the dimensionality of the system. As a three-dimensional system is considered for the MD simulations, $\alpha = 3$.

An additional finite-size-effect correction [62,63] was added to obtain the final diffusivity. The transport properties and long-range corrections of water and LJ fluids are system-size dependent. The diffusion of these particles is influenced not only by hydrodynamic interactions with the surrounding solvent but also by interactions with periodic images of the particles and the solvent itself, leading to an underestimation of the diffusion coefficients. To account for this behavior, a correction term incorporating system-size dependence was employed as

$$D_i = D_i' + \frac{k_B T \zeta}{6\pi\eta L} \tag{32}$$

where D_i represents the diffusivity of the species corrected for finite-size effects, k_B represents the Boltzmann constant, T is the temperature of the system, ζ is a dimensionless number equal to 2.84 for a cubic simulation box, η represents the dynamic viscosity of the system from ref. [56], and L represents the average length of the simulation box, which was 53.4 Å.

III. RESULTS AND DISCUSSION

The full model described above was first solved for four operating temperatures: 25, 40, 60, and 80°C with a fixed diffusivity of the ionic species. These results, presented in Sec. III A, show a contradiction between the typical experimentally observed behavior of current density and changes in operating temperature. To rectify the gap, we ran MD simulations to determine the diffusion coefficients of the participating ions as a function of the operating temperature, findings of which are detailed in Sec. III B. Section III C subsequently presents the full-model predictions in the range of cell potentials varying from 1.3 to 1.8 V at an interval of 0.05 V, considering the temperature-dependent diffusivity of ions.

Later, in Sec. III D, we elaborate on the contributions of the molecular modes of transport of ionic species (diffusion and migration) toward the total electrical current across the electrode gap. Further, in Secs. III E and III F, we present a discussion on the variation of the electrolyte conductivity perpendicular to the electrodes and of the current distribution along the electrode height due to nonuniformity in the electrolyte resistances. These discussions examine the effects of electroneutrality in the electrolyte, the gas-phase volume fraction near the electrodes, the thickening of the boundary layer downstream, and the gradients in the concentration distribution of the OH^- ions.

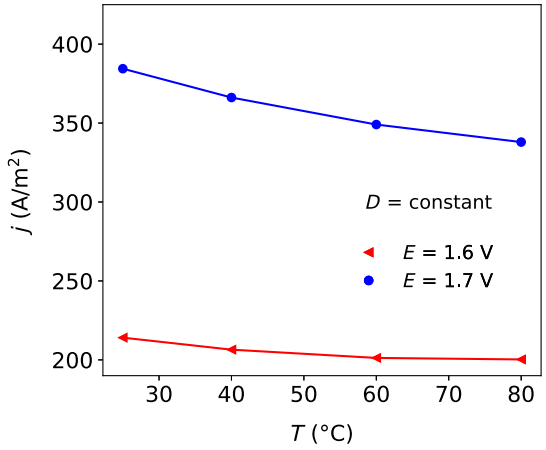

FIG. 2. Variation of the average current density (j) across the AWE cell with respect to the operating temperature (T) at fixed cell potential differences, predicted with a constant diffusivity of ions ($D_{0,K^+} = 1.92 \times 10^{-9}$ m^2/s and $D_{0,OH^-} = 5.27 \times 10^{-9}$ m^2/s).

A. Predictions with constant diffusivity of ions

Figure 2 presents the model-predicted average current density output for two cell potentials, $E = 1.6$ and 1.7 V, with the diffusivity of ions kept fixed across the temperature range. The COMSOL simulations were carried out for four temperatures, 25, 40, 60, and 80°C. The figure indicates that the performance of the electrolyzer would diminish with an increase in the operating temperature. At 1.6 V, the ratio of current density at 80°C to that at 40°C is 0.96, while at 1.7 V, this ratio is 0.92.

However, the ratio of the current density from experimental measurements for the same enhancement in the operating temperature is noted to be > 1 (at a constant cell potential) [7,64]. This clearly demonstrates a contradiction between the model predictions and experimental measurements. In other words, it shows a flipped trend of the overall performance change with an increase in temperature. Later, we show that the reason for this disagreement is the neglected dependence of the diffusivity of the ionic species on the system temperature. According to the definition of ionic mobility and for constant D values, the mobility decreases with increasing temperature. This results in a lower electrolyte conductivity and, therefore, higher Ohmic losses across the cell. Hence, the electromigration component of the total current across the cell decreases with an increase in temperature. We revisit these arguments in Sec. III C to corroborate our observations.

B. Ionic diffusivity from MD simulations

MD simulations were conducted at various temperatures (25, 40, 50, 60, 70, and 80°C) to obtain the diffusivity values for potassium (K^+) and hydroxide (OH^-) ions. In Fig. 3, we depict the obtained values of the diffusivity of the ions. The values show the expected increase in the diffusivity values with an increase in the temperature of

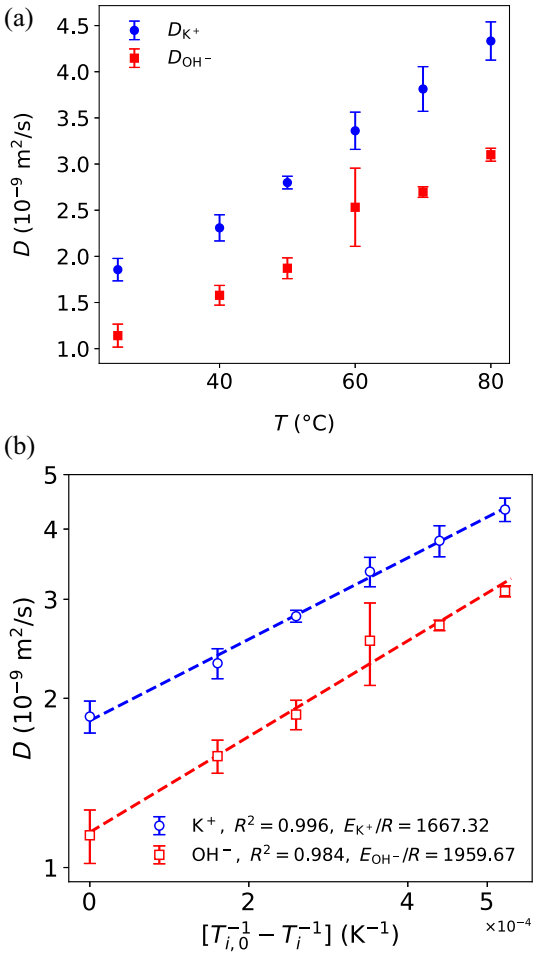

FIG. 3. Temperature dependence of ion diffusivities. (a) Diffusion coefficients of OH^- and K^+ ions at different temperatures obtained from MD simulations. (b) The profiles in (a) fit to an exponential function similar to the Arrhenius equation to obtain the scaled activation barrier (in K) E^D/R.

the electrolyte solution. To quantify the dependence of the diffusivity values on the operating temperature, an exponential equation, similar to the Arrhenius equation, was fitted for both ions individually. Equation (33) below shows the equation used

$$D(T) = D_0(T_0)e^{-\frac{E_i^D}{R}\left(\frac{1}{T}-\frac{1}{T_0}\right)}, \tag{33}$$

where $D(T)$ is the diffusivity of the ion at temperature T, T_0 denotes the reference temperature, E^D is the activation barrier for diffusion, and R is the gas constant. Taking the logarithm of both sides of the equation, we get

$$\ln(D(T)) = \frac{E^D}{R}\left(\frac{1}{T_0} - \frac{1}{T}\right) + \ln(D_0) \tag{34}$$

Now, by considering $X = (\frac{1}{T_0} - \frac{1}{T})$ and $Y = \ln(D(T))$, one obtains the equation for a straight line as

TABLE IV. Calculated diffusivity of K^+ and OH^- ions at various temperatures using Eq. (33) with the respective experimentally reported diffusivity at 25 °C and the MD-predicted diffusion activation barrier.

T °C	D_{K^+} (m^2/s)	D_{OH^-} (m^2/s)
25	1.96×10^{-9}	5.27×10^{-9}
40	2.56×10^{-9}	7.22×10^{-9}
50	3.02×10^{-9}	8.77×10^{-9}
60	3.530×10^{-9}	1.05×10^{-8}
70	4.08×10^{-9}	1.25×10^{-8}
80	4.69×10^{-9}	1.47×10^{-8}

$$Y = MX + C, \tag{35}$$

where $M = \frac{E^D}{R}$ and $C = \ln(D_0)$.

Figure 3(b) shows the plots discussed in Eqs. (34) and (35) for K^+ and OH^- ions, depicting an excellent fit with $R^2 \approx 1$ for both ionic species. Though in the present work, the electrolyte concentration was not varied, an increase in concentration of KOH increases ion-ion and ion-ion solvent interactions, which leads to a higher solution viscosity and a reduction in the diffusivity of ions [56]. Thus, the value of the slope M (i.e., the apparent activation energy) is not a universal parameter.

The scaled activation barrier, $M = E^D/R$, estimated from this exercise, was then used to determine the diffusivity of ions at various temperatures by employing the experimentally reported values of diffusivity at 25°C, at which, $D_{0,K^+} = 1.96 \times 10^{-9}\ m^2/s$ and $D_{0,OH^-} = 5.27 \times 10^{-9}\ m^2/s$ [34]. Note that hydroxide ions diffuse faster than potassium ions in experiments. Although MD simulations predict the reverse trend, they are used here solely to determine the respective diffusion activation barrier. The uncertainty in the MD-derived diffusivities was assessed using the upper and lower bounds obtained from independent simulations, and the corresponding variation in predicted current density was found to be approximately 13%–20%. The values of the diffusivity of the ions obtained for different temperatures are tabulated in Table IV.

In the next section, we discuss the predicted output of the electrolyzer based on the full-scale simulations with the diffusivity of ions varying with the operating temperature at 40, 60, and 80°C.

C. Predictions with temperature-dependent diffusivity of ions

Figure 4(a) presents the current density-temperature profiles for different applied cell potentials. The predictions show that an increase in temperature results in a higher current flowing across the cell. The trends agree well with reported measurements for isothermally operated cells [7,64]. The ratio of current density at 80 to 40°C

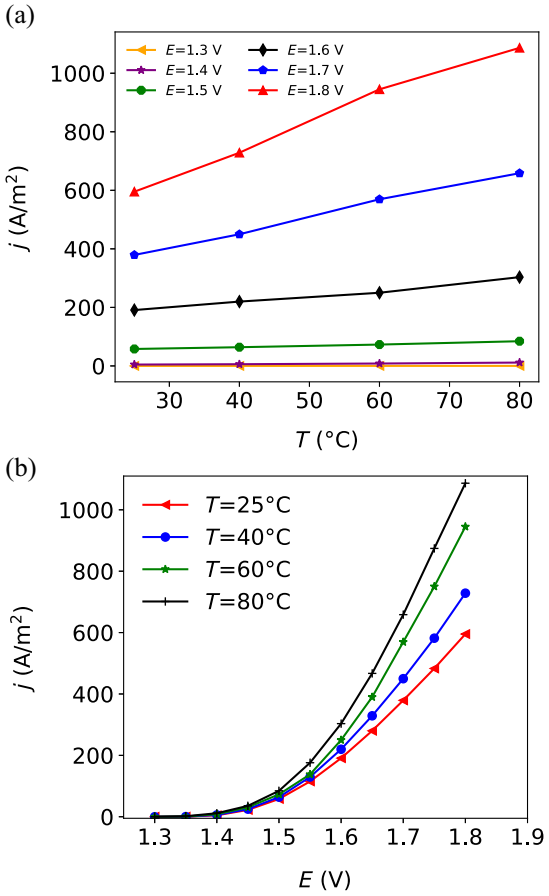

FIG. 4. Variation of the average current density (j) across the AWE cell predicted from the model simulations considering temperature-dependent diffusivity of ions with respect to changes in (a) operating temperature (T) at fixed cell potential difference and (b) cell potential (E) at fixed operating temperature.

is about 1.38 for 1.6 V and 1.46 for 1.7 V. The corresponding polarization curves (current density vs cell potential) are presented in Fig. 4(b). The values depict an exponential increase in the current density with an increase in the cell potential, attributable to the exponential dependence of the current density on the activation overpotential through the Butler-Volmer kinetics.

Interestingly, the effect of the operating temperature on the overall yield is multifaceted. Notably, the current density magnitudes show differential extents of increase with temperature, depending on the imposed cell potential. For low cell potentials (1.3–1.4 V), the slope of the profiles is nearly zero, marking a negligible increment with temperature, which for moderate magnitudes of cell potential (1.5–1.6 V) increases only slightly. For the higher voltage regime (1.7–1.8 V), the increase in current density is significant, so much so that the current density increases by more than 1.7 times (from 379.2 to 658.4 A m^{-2} at 1.7 V and from 595.3 to 1086.7 A m^{-2} at 1.8 V) when the operating temperature increases from

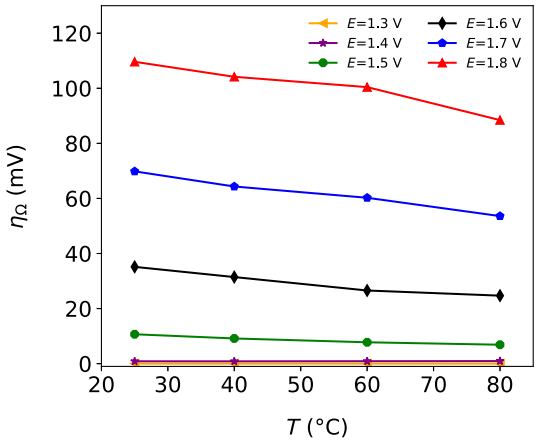

FIG. 5. Variation of the Ohmic overpotential (η_Ω) at different operating temperatures.

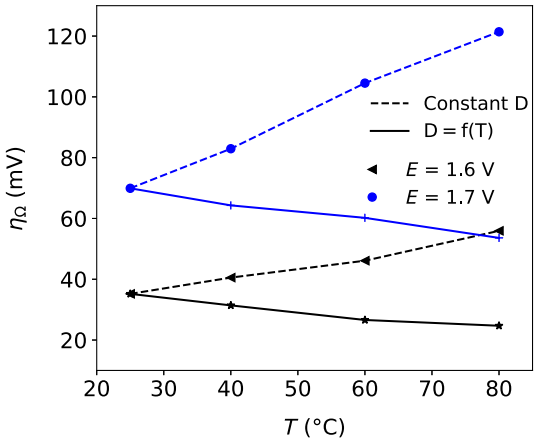

FIG. 6. Comparison of the Ohmic overpotential (η_Ω) at different operating temperatures for the two cases, with the diffusivity of the ions assumed constant or varying with the change in the operating temperature.

25 to 80°C. An increase in temperature is associated with a lowering of charge-transfer resistances (a lower activation overpotential is needed for fixed currents, or larger currents can be sustained at the same overpotential) as well as increased diffusivity of the participating ions, leading to a reduced Ohmic overpotential [47]. The latter has no bearing on the charge-transfer resistance and would decrease with an increase in temperature. However, as the effective Ohmic overpotential also depends on the total current, it varies in response to changes in temperature in a complex manner.

The Ohmic overpotential is the potential drop across the electrolyte since this energy is required for ionic migration between the two electrodes. Here, we estimated the Ohmic overpotential for each half-cell (η_Ω) using Eq. (20), assuming $\nabla c_i = 0$ everywhere. The potential gradient thus obtained was converted to the potential drop using the half-cell width of 2 mm. The estimate as a function of temperature is shown in Fig. 5. It can be seen that the overpotential remains fairly constant for low potentials (1.3–1.4 V). In other words, the operations remain kinetically controlled. The intermediate cell potentials lie in the transition regime, where it can be said that the cell experiences a mixed control of kinetics and mass transport. At high cell potentials, when the cell current density is roughly two orders higher, the mass transport losses contribute significantly. The figure shows that Ohmic overpotential decreases by 20%–35% when the temperature is increased from 25 to 80°C.

A similar analysis for the Ohmic overpotential (η_Ω) was carried out for the cases where the diffusivity of the ions was kept fixed (Sec. III A). Figure 6 corroborates that the observed inconsistency in the model predictions with respect to the average current density (Fig. 2) is indeed because the Ohmic losses appear to increase with an increase in the operating temperature, attributable to the decrease in ionic mobility.

The observed trends for changes in the output current density with temperature and cell potential are a result of variations in the constitutive fluxes of ions across the cell width. In the next section, we analyze the contribution of the molecular-scale transport modes (diffusion and migration) and their variation near the electrodes, all in the context of changes in the operating temperature. To keep the discussion incisive in the rest of the paper, we limit it to the results obtained for 1.7 V cell potential and operating temperatures 40, 60, and 80°C, while all other parameters are held constant. The findings should hold true with proportionate variations for other operating conditions.

D. Current distribution across the electrode gap

Figure 7(a) presents the magnitude of the migration component of the averaged current density ($\mathbf{j}_{\text{migration}}$) in the electrolyte near electrodes in both half-cells for 40, 60, and 80°C at $E = 1.7$ V. Figure 7(b) presents the migration and diffusion components of the current density for only the highest temperature case. The H_2 gas-producing cathodic side is labelled as the HER half-cell. Similarly, the anodic side, where O_2 gas is produced, is labeled as the OER half-cell. The profiles are presented for 0.5 mm distance perpendicular to the electrode (in the x direction) plotted at half of the electrode height (at $y = 50$ mm).

The factors contributing to the current density at any point are described by Eq. (19). The convective mode of bulk transport in the electrolyte does not contribute to the electrical current due to the applied local electroneutrality condition [47]. Thus, the forced convection of the electrolyte only indirectly contributes to the total flux by modulating the concentration distribution of the ions. The continuous pumping of the electrolyte, with only a fraction of it being split into constituent ions, also eliminates concentration gradients in the bulk of the half-cells. Hence, at very small distances from the electrodes, the diffusive

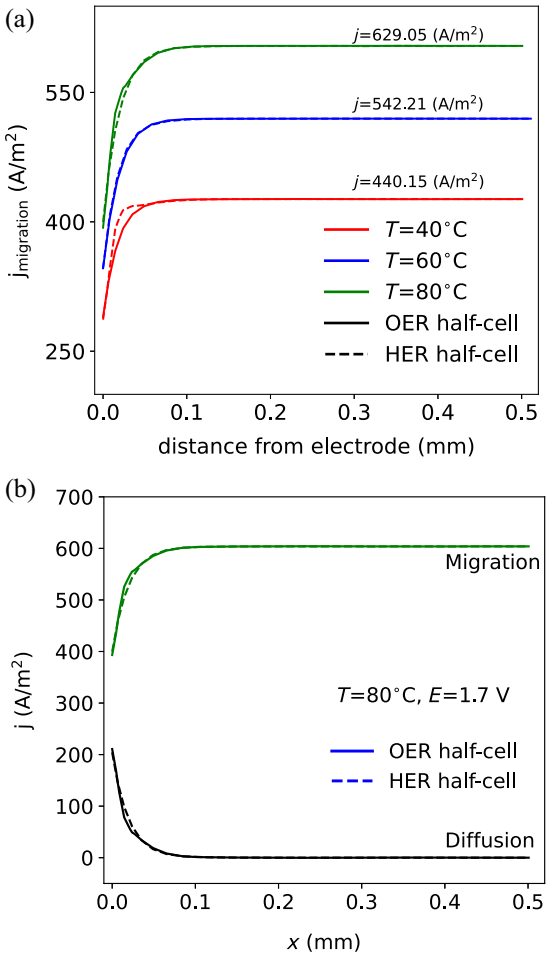

FIG. 7. Components of the ionic current at various temperatures. (a) Spatial variation of the migration component of the total current density ($\mathbf{j}_{\text{migration}}$) across the electrode gap at $T = 40$, $T = 60$, and $T = 80$°C. (b) Migration and diffusion current density components for $T = 80$ °C. The cell potential difference (E) is = 1.7 V and the profiles are plotted at the middle height of the cell ($y = 50$ mm).

fluxes become zero. This behavior remains invariant across the cell width, including the separator. Hence, the only active mode of ionic transport in the majority of the cell width is migration. It occurs in response to the active electric field and is governed by the electrolyte conductivity. These characteristics hold for any set of cell potential or operating temperature values.

The effect of the change in the operating temperature is evidenced by an increase in the total current density from 440.2 to 629.0 A m^{-2} with an increase in temperature from 40 to 80°C. At the intermediate temperature of 60°C, the averaged current density is 542.2 A m^{-2}. This is also depicted by changes in the migration component in the bulk, where the value of migration current density exactly matches the total current density.

In regions close to the electrodes, the diffusive component starts playing a decisive role. The HER electrode releases OH^- ions while the counter electrode consumes them to generate O_2. The existing concentration gradients contribute to the movement of OH^- and K^+ ions near the electrode, and therefore, correspondingly, the migration component reduces. The total current passing thus is split into two molecular-scale constitutive modes. Figure 7(b) highlights this effect for 80°C, where we also see that the two electrodes show asymmetry in the diffusive and migration components of the current. The HER half-cell shows a steeper gradient with a much thinner concentration boundary layer. Recall that the migration current is governed by both the local electrolyte conductivity and the electrical field in the electrolyte according to

$$\mathbf{j}_{\text{migration}} = \kappa(-\nabla\phi_l).$$

At 40°C, the electrolyte conductivity and ionic diffusivity are relatively low, resulting in slower ion transport through the electrolyte. Under these conditions, OH^- replenishment near the OER electrode becomes slower due to the continuous consumption of hydroxide ions during oxygen evolution. Consequently, the migration current stabilizes earlier near the HER side, whereas a more gradual variation is observed near the OER side due to the relatively larger local transport resistance. This leads to asymmetry in the migration current profiles. At 60°C, the increase in ionic mobility, diffusivity, and conductivity improves ion transport throughout the cell. As a result, the migration current profiles become nearly symmetric, with similar stabilization behavior on both sides. At 80°C, although conductivity and diffusivity increase further, the electrochemical reaction rates also become significantly higher, especially near the HER electrode. The resulting increase in hydrogen bubble generation locally disrupts ion transport and reduces the effective electrolyte area available for ion conduction near the HER side. Therefore, the migration current stabilizes earlier near the OER side, while delayed stabilization near the HER side produces a mild asymmetry in the migration current profiles.

The correlation used for electrolyte conductivity as a function of temperature in the literature subsumes these effects through the fitting of the observed trends [65]. We have quantitatively compared the ionic conductivities obtained from our MD-based diffusivities. The trends with temperature change agree well, though our estimates of conductivities are higher by a factor of about 1.3–1.45 over the investigated temperature range.

However, our predictions, based on MD-predicted diffusion coefficients, not only depict the behavior of measurements correctly but also reinforce the fact that the diffusive behavior is more sensitive to temperature than just exhibiting a linear dependency and that the correct accounting of transport resistances is critical in understanding the working of AWEs and their optimization.

The asymmetry in the gas-phase volume fraction in the two half-cells, which gives rise to the characteristic behavior of the current density components, also affects the local electrolyte conductivity asymmetrically and thus distributes the Ohmic resistances unequally. We next analyze these features for the electrolyte conductivity as it varies across the cell width and also along the flow direction.

E. Understanding variations in electrolyte conductivity

The presence of the gas phase near the electrodes decreases the local electrolyte conductivity. Our model quantifies it using Bruggeman's relation by incorporating the spatial distribution of the gas-phase volume fraction [Eq. (19)]. The spatial variations in the electrolyte conductivity are presented in Fig. 8 at cell potential $E = 1.7$ V for the three temperatures. The profiles are plotted perpendicular to the electrodes in the HER and the OER half-cells at four different points along the height of the electrodes ($y = 30$, 50, 80, and 100 mm).

In the bulk of both half-cells, where ϕ_c becomes unity, the electrolyte conductivity assumes its uncorrected value. With a change in the operating temperature, its magnitude changes from 35.0 S/m at 40°C to 48.1 S/m and to 61.4 S/m at 60 and 80°C, respectively. This is a direct outcome of the increase in the mobility of the ions, though in the definition [see Eq. (16)], the temperature is in the denominator. With no concentration gradients and $\phi_d = 0$, the electrolyte exhibits the same conductivity in the bulk along the flow direction. In the separator, $\phi_c = 0.3$, and in response, the electrolyte conductivity decreases to a different constant magnitude.

Close to the electrodes, where concentration gradients in the x-direction persist and gradually change in response to the thickening of the boundary layers and accumulation of gas bubbles downstream, the electrolyte solution exhibits spatially varying conductivity. The effect is evident at all points, where the conductivity values approach the bulk value at distances farther away in x with more distance covered in y direction. Thus, the conductivity undergoes its most significant reduction near the outlet for both electrodes. At 40°C, the drop in conductivity is about 33%, while at 60 and 80°C, the drop is about 39% and 50%, respectively.

This is an involved outcome for the existing concentration gradients and the gas-phase volume fraction. At the HER electrode, OH^- ions are produced, and the concentration is the highest near the electrode. At 40 and 80°C, the highest concentration magnitude predicted at $y = 50$ mm height is 1018 and 1009 mol m^{-3}, respectively. Higher ionic concentrations increase the electrical conductivity. This behavior, coupled with twice the gas phase volume fraction in the HER half-cell, diminishes the conductivity far more than what is seen in the OER

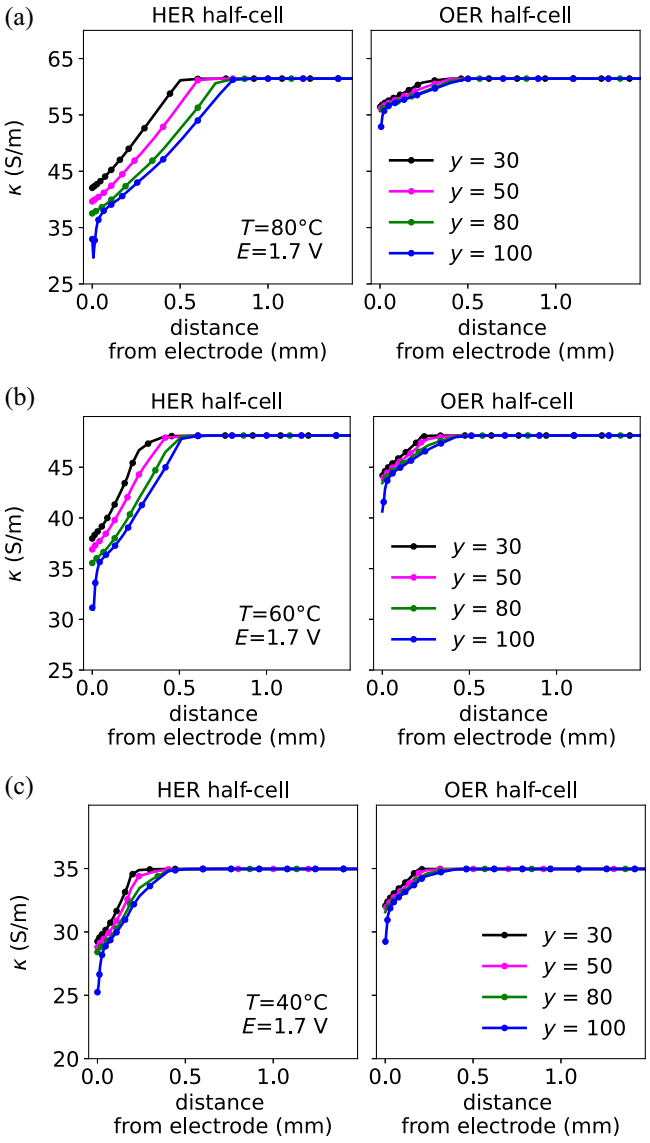

FIG. 8. Variation of the electrolyte conductivity in the downstream direction at different heights for operating temperatures of (a) 80°C, (b) 60°C, and (c) 40°C.

half-cell. At the same vertical height, the OER electrode sees the concentration of 978 mol m^{-3} at 40 °C and 986 mol m^{-3} at 80°C. The prevailing concentration fields and the gas phase act in tandem to decrease the conductivity. The trends at 60°C fall in between these two extremes. The concentration field for K^+ ions exactly follows the field for OH^- ions, given that the electroneutrality condition is applicable everywhere.

The asymmetry in the local electrolyte conductivity, coming from the distribution of the gas phase volume fraction and its increase along the flow direction, results in a nonuniform current distribution along the electrode length. We analyze this next in the context of a change in the operating temperature.

F. Understanding the current density variation along the electrode height

To elaborate on the nonuniformity in the current density distribution along the y-direction, we plot the "mid-separator" current density ($j_{x=2.5\ \mathrm{mm},y}$). It refers to the current density measured at the plane midway between the anode and cathode ($x = 2.5$ mm). Figure 9 shows its profile scaled with the current density at the leading edge of the cell $j_{x=2.5\ \mathrm{mm},y=0}$. Since current is a conserved quantity, the current density across the electrode gap at any plane in y remains the same, and its magnitude is decided by the rate-determining resistance. The metal electrodes, having high electrical conductivity, behave as equipotential surfaces and do not contribute to the observed nonuniformity.

The profiles exhibit a monotonic decrease from the bottom to top of the cell, indicating that the lower regions of the electrodes (leading edge, $y = 0$) experience higher current density compared to the upper regions. At 40°C, the normalized current density decreases by approximately 3% from the bottom to the top, whereas at 80°, the reduction is to about 94%, indicating a more dispersed current distribution. As expected and following the observed trend everywhere, the decrease is of about 4% at 60°C. This nonuniformity primarily arises due to spatial variations in the gas-phase volume fraction (ϕ_d) along the electrode, as ultimately governed by the hydrodynamics of the boundary layers so formed. While a higher temperature is associated with enhanced ionic mobility, the higher current density intensifies gas evolution rates. With the gradual decay in the momentum of the electrolyte flowing near the electrode surfaces, ϕ_d increases. In terms of physical understanding, the accumulated bubbles obstruct ion-conducting pathways and increase the local electrical resistance. The bottom region, which is less hindered by gas accumulation, maintains a thinner boundary layer.

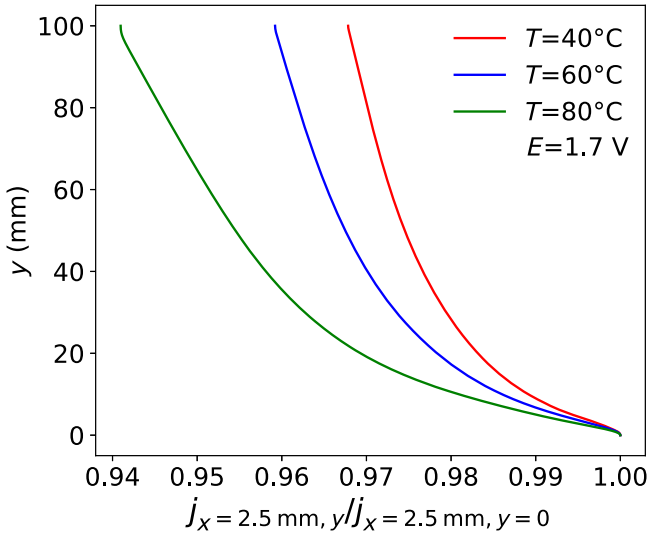

FIG. 9. Mid-separator current density at $T = 40$°C and $T = 80$°C at $E = 1.7$ V.

IV. CONCLUSIONS

In this work, we presented a continuum modeling framework coupled with molecular simulations of temperature-dependent ion diffusivities that offers a panoramic understanding of transport modes in alkaline water electrolyzers (AWEs) and their associated resistances with precise quantification. The model captures the effect of changes in the operating temperature on the overall performance of AWEs through a detailed description using the Nernst-Planck ion-transport and Euler-Euler laminar-flow formulations to account for, respectively, the current distribution and the presence of two fluid phases in the electrolyte. This allows one to take into consideration spatially distributed bulk and molecular-scale transport modes (diffusion and migration) within an interpenetrating liquid-gas electrolyte phase. Predictions consistent with prior experimental findings are only made when temperature-dependent diffusion coefficients of the participating ions, as determined using molecular dynamics simulations, are incorporated into the continuum model. In this scenario, elevated temperatures show both enhanced electrochemical kinetics and increased ionic mobility, effectively leading to higher current density yield. Nevertheless, the resulting increased gas-phase volume fraction counteracts the favorable kinetics and transport rates. On the other hand, a constant diffusivity value (independent of temperature) leads to severe ion-transport limitations, leading to a reduction in the overall current density as a function of temperature, contrary to prior experimental findings.

The insights from the model reveal that the overall working of AWEs is fairly complex and is markedly affected by the mass transport capabilities of the system; the effects are compelling at higher operating cell voltages, when large current densities are predicted across the cell width (>400 A m^{-2}). In this regime, the mass transport resistances determine the overall output. The presence of differential amounts of gas phases in the two half-cells, distinct diffusion coefficients of OH^- and K^+ ions, and the entrainment of bubbles in the boundary layers whose thickness increases along the flow direction render an asymmetric distribution of the resistances in the two half-cells. From these nonuniform resistance profiles across the anode and cathode chambers, as noted through the diffusive and migrational components of the total current density and of the local electrolyte conductivity profiles, emerges nonuniformity in the current distribution in the downstream direction.

The findings underscore the need to address individually the transport and kinetic details of both half-cells as a function of temperature. The inclusion of more rigorous details, such as gas bubble dynamics (nucleation, growth,

and detachment), might offer detailed insights into local and temporal changes in electrolyte properties [66] and can be combined with the full cell-scale model to get a unified framework. Further, the present MD-continuum model can be augmented with more accurate charge-transfer parameters (electrochemical kinetics and electrical double-layer properties) derived from quantum-mechanical calculations. Nevertheless, the insights from our temperature-dependent model provide a foundational framework for future experimental and computational efforts aimed at the rational design and scale-up of high-performance AWE systems.

ACKNOWLEDGMENTS

A. T. acknowledges a Ph.D. fellowship from the Ministry of Education, Government of India, and an M.Tech. Fellowship from Shell India Markets Pvt. Ltd., which supported some of her earlier work in this area. The authors acknowledge discussions with Dr. Shauvik De and Dr. Durai Palanisamy from Shell India Markets Pvt. Ltd. on multiscale modeling of AWEs. The authors also acknowledge I-STEM for providing the licensing support for COMSOL Multiphysics. We thank Dr. Abhijit Gogoi for his technical assistance in carrying out MD simulations.

The authors declare no conflicts of interest.

DATA AVAILABILITY

The data that support the findings of this article are not publicly available upon publication because it is not technically feasible and/or the cost of preparing, depositing, and hosting the data would be prohibitive within the terms of this research project. The data are available from the authors upon reasonable request.

[1] P. A. Kempler, R. H. Coridan, and L. Luo, *Gas evolution in water electrolysis*, Chem. Rev. **124**, 10964 (2024).

[2] Q. Feng, X.-Z. Yuan, G. Liu, B. Wei, Z. Zhang, H. Li, and H. Wang, *A review of proton exchange membrane water electrolysis on degradation mechanisms and mitigation strategies*, J. Power Sources **366**, 33 (2017).

[3] M. A. Laguna-Bercero, *Recent advances in high temperature electrolysis using solid oxide fuel cells: A review*, J. Power Sources **203**, 4 (2012).

[4] K. Hu, J. Fang, X. Ai, D. Huang, Z. Zhong, X. Yang, and L. Wang, *Comparative study of alkaline water electrolysis, proton exchange membrane water electrolysis and solid oxide electrolysis through multiphysics modeling*, Appl. Energy **312**, 118788 (2022).

[5] T. Zhang, Y. Liu, Q. Ye, and H. J. Fan, *Alkaline seawater electrolysis at industrial level: Recent progress and perspective*, J. Electrochem. **28**, 2214006 (2022).

[6] B. Yang, R. Zhang, Z. Shao, and C. Zhang, *The economic analysis for hydrogen production cost towards electrolyzer technologies: Current and future competitiveness*, Int. J. Hydrog. Energy **48**, 13767 (2023).

[7] R. A. Marquez, M. Espinosa, E. Kalokowski, Y. J. Son, K. Kawashima, T. V. Le, C. E. Chukwuneke, and C. B. Mullins, *A guide to electrocatalyst stability using lab-scale alkaline water electrolyzers*, ACS Energy Lett. **9**, 547 (2024).

[8] A. Govind Rajan, J. M. P. Martirez, and E. A. Carter, *Coupled effects of temperature, pressure, and pH on water oxidation thermodynamics and kinetics*, Acs Catal. **11**, 11305 (2021).

[9] R. A. Marquez, J. T. Bender, A. M. Aleman, E. Kalokowski, T. V. Le, C. L. Williamson, M. L. Frederiksen, K. Kawashima, C. E. Chukwuneke, and A. Dolocan, *Insights into catalyst degradation during alkaline water electrolysis under variable operation*, Energy Environ. Sci. **18**, 7170 (2025).

[10] X. Lu and C. Zhao, *Electrodeposition of hierarchically structured three-dimensional nickel–iron electrodes for efficient oxygen evolution at high current densities*, Nat. Commun. **6**, 6616 (2015).

[11] H. Zhou, F. Yu, Q. Zhu, J. Sun, F. Qin, L. Yu, J. Bao, Y. Yu, S. Chen, and Z. Ren, *Water splitting by electrolysis at high current densities under 1.6 volts*, Energy Environ. Sci. **11**, 2858 (2018).

[12] B. K. Kang, S. Y. Im, J. Lee, S. H. Kwag, S. B. Kwon, S. N. Tiruneh, M.-J. Kim, J. H. Kim, W. S. Yang, B. Lim, and D. H. Yoon, *In-situ formation of MOF derived mesoporous* CO_3 N*/amorphous N-doped carbon nanocubes as an efficient electrocatalytic oxygen evolution reaction*, Nano Res. **12**, 1605 (2019).

[13] K. C. Sandeep, S. Kamath, K. Mistry, M. A. Kumar, S. K. Bhattacharya, K. Bhanja, and S. Mohan, *Experimental studies and modeling of advanced alkaline water electrolyser with porous nickel electrodes for hydrogen production*, Int. J. Hydrog. Energy **42**, 12094 (2017).

[14] I. E. Dincer and M. Agelin-Chaab, *Experimental investigation and evaluation of newly designed electrodes for hydrogen production in alkaline water electrolysis*, J. Power Sources **632**, 236326 (2025).

[15] A. K. Verma, S. Atif, A. Padhy, T. S. Choksi, P. Barpanda, and A. Govind Rajan, *Robust oxygen evolution on Ni-doped* MoO_3*: Overcoming activity–stability trade-off in alkaline water splitting*, Chem. Bio Eng. **2**, 241 (2025).

[16] M.-A. Babay, M. Adar, A. Chebak, and M. Mabrouki, *Enhancing proton exchange membrane fuel cell efficiency: Optimal tilt angles and airflow dynamics in wedge-shaped flow channels*, Fuel **397**, 135447 (2025).

[17] R. Wang, S. Yuan, R. Xue, M. Cheng, X. Yan, S. Shen, Y. Guo, and J. A. Zhang, *A 3D numerical study on flow field designs in zero-gap* CO_2 *electrolyzers*, Energy Fuels **39**, 3942 (2025).

[18] N. Shang, H. Wang, K. Wang, R. Zhang, D. Zhong, M. Wei, and P. Pei, *A high power flexible Zn-air battery via concurrent PAA modulation and structural tuning*, Energy Storage Mater. **74**, 103923 (2025).

[19] P. Olivier, C. Bourasseau, and P. B. Bouamama, *Low-temperature electrolysis system modelling: A review*, Renew. Sustain. Energ Rev. **78**, 280 (2017).
[20] C. Daoudi and T. Bounahmidi, *Overview of alkaline water electrolysis modeling*, Int. J. Hydrog. Energy **49**, 646 (2024).
[21] Ø. Ulleberg, *Modeling of advanced alkaline electrolyzers: A system simulation approach*, Int. J. Hydrog. Energy **28**, 21 (2003).
[22] E. Amores, J. Rodríguez, and C. Carreras, *Influence of operation parameters in the modeling of alkaline water electrolyzers for hydrogen production*, Int. J. Hydrog. Energy **39**, 13063 (2014).
[23] M. Sánchez, E. Amores, L. Rodríguez, and C. Clemente-Jul, *Semi-empirical model and experimental validation for the performance evaluation of a 15 kW alkaline water electrolyzer*, Int. J. Hydrog. Energy **43**, 20332 (2018).
[24] A. Ursúa and P. Sanchis, *Static–dynamic modelling of the electrical behaviour of a commercial advanced alkaline water electrolyser*, Int. J. Hydrog. Energy **37**, 18598 (2012).
[25] J. Rodríguez and E. Amores, *CFD modeling and experimental validation of an alkaline water electrolysis cell for hydrogen production*, Processes **8**, 1634 (2020).
[26] H. Muhsen, M. Alshawabkeh, M. Al-Mahmodi, A. Ghanem, and A. Al-Halhouli, *Sensitivity analysis of electrodes spacing media for evaluating alkaline electrolyzer performance through CFD modeling*, Renew. Energy Focus **49**, 100575 (2024).
[27] A. Zarghami, N. G. Deen, and A. W. Vreman, *CFD modeling of multiphase flow in an alkaline water electrolyzer*, Chem. Eng. Sci. **227**, 115926 (2020).
[28] W. A. El-Askary, I. M. Sakr, K. A. Ibrahim, and A. Balabel, *Hydrodynamics characteristics of hydrogen evolution process through electrolysis: Numerical and experimental studies*, Energy **90**, 722 (2015).
[29] P. Mandin, A. A. Aissa, H. Roustan, J. Hamburger, and G. Picard, *Two-phase electrolysis process: From the bubble to the electrochemical cell properties*, Chem. Eng. Process. Process Intensif. **47**, 1926 (2008).
[30] A. Sokolichin, G. Eigenberger, A. Lapin, and A. Lübert, *Dynamic numerical simulation of gas-liquid two-phase flows Euler/Euler versus Euler/Lagrange*, Chem. Eng. Sci. **52**, 611 (1997).
[31] M. D. Mat, K. Aldas, and O. J. Ilegbusi, *A two-phase flow model for hydrogen evolution in an electrochemical cell*, Int. J. Hydrog. Energy **29**, 1015 (2004).
[32] M.-A. Babay, M. Adar, A. Chebak, and M. Mabrouki, *Dynamics of gas generation in porous electrode alkaline electrolysis cells: An investigation and optimization using machine learning*, Energies **16**, 5365 (2023).
[33] A. Sirat, S. Ahmad, I. Ahmad, N. Ahmed, and M. Ahsan, *Integrative CFD and AI/ML-based modeling for enhanced alkaline water electrolysis cell performance for hydrogen production*, Int. J. Hydrog. Energy **83**, 1120 (2024).
[34] A. J. Bard, L. R. Faulkner, and H. S. White, *Electrochemical Methods: Fundamentals and Applications* (John Wiley & Sons, New York, 2022).
[35] R. Kanemoto, T. Araki, R. Misumi, and S. Mitsushima, *Numerical modeling of two-phase flow considering multiple bubble sizes in an alkaline water electrolyzer*, Chem. Eng. Sci. **304**, 120986 (2025).
[36] M. A. Ansari, S. Srivastava, and S. Kumar, *Designing isothermal natural convection dominated electrochemical cells: experimental validation*, Ind. Eng. Chem. Res. **63**, 22422 (2024).
[37] P. A. Boettcher, E. Agar, C. R. Dennison, and E. C. Kumbur, *Modeling of ion crossover in vanadium redox flow batteries: A computationally-efficient lumped parameter approach for extended cycling*, J. Electrochem. Soc. **163**, A5244 (2015).
[38] M. R. Singh, J. D. Goodpaster, A. Z. Weber, M. Head-Gordon, and A. T. Bell, *Mechanistic insights into electrochemical reduction of* CO_2 *over Ag using density functional theory and transport models*, Proceed. Natl. Acad. Sci. U.S.A. **114**, E8812 (2017).
[39] See Supplemental Material at http://link.aps.org/supplemental/10.1103/8zs3-7ynk for detailed justification of constant bubble size and isothermal assumptions, which includes Ref. [40], and the mean-squared displacement plots for the OH^- and K^+ ions, obtained for five independent runs.
[40] R. B. Bird, W. E. Stewart, and E. N. Lightfoot, *Transport Phenomena*, Revised 2nd ed. (John Wiley & Sons, New York, 2007).
[41] M. Zhang, L. Gao, L. Yang, G. Shan, Y. Wang, X. Huo, W. Li, and J. Zhang, *Temperature distribution evolution in zero-gap alkaline water electrolyzer: Experimental and modeling*, Fuel **367**, 131418 (2024).
[42] D. Le Bideau, P. Mandin, M. Benbouzid, M. Kim, M. Sellier, F. Ganci, and R. Inguanta, *Eulerian two-fluid model of alkaline water electrolysis for hydrogen production*, Energies **13**, 3394 (2020).
[43] Y. Xia, M. Gao, J. Yu, Y. Si, L. Chen, and S. Numerical Mei, *Study on hydrodynamic characteristics and electrochemical performance of alkaline water electrolyzer by micro-nano surface electrode*, Materials **15**, 4927 (2022).
[44] M. Ishii and N. Zuber, *Drag coefficient and relative velocity in bubbly, droplet or particulate flows*, AIChE J. **25**, 843 (1979).
[45] Y. Liu, S. Li, H. Wu, and Y. Shi, *Experimental investigation and analysis for the bubble size distribution during alkaline water electrolysis by using a wire electrode*, DeCarbon **5**, 100052 (2024).
[46] R. Wedin and A. A. Dahlkild, *On the transport of small bubbles under developing channel flow in a buoyant gas-evolving electrochemical cell*, Ind. Eng. Chem. Res. **40**, 5228 (2001).
[47] J. Newman and N. P. Balsara, *Electrochemical Systems* (John Wiley & Sons, New York, 2021).
[48] V. R. Raghavan, and H. Martin, *Modelling of two-phase thermal conductivity*, Chem. Eng. Process. Process Intensif. **34**, 439 (1995).
[49] COMSOL Multiphysics® Electrochemical Heating—Battery Module (2020), Accessed: July 20, 2025, https://doc.comsol.com/5.6/doc/com.comsol.help.battery/battery_ug_electrochem.07.003.html.

[50] R. L. LeRoy, C. T. Bowen, and D. J. LeRoy, *The thermodynamics of aqueous water electrolysis*, J. Electrochem. Soc. **127**, 1954 (1980).

[51] S. Haussener, C. Xiang, J. M. Spurgeon, S. Ardo, N. S. Lewis, and A. Z. Weber, *Modeling simulation, and design criteria for photoelectrochemical water-splitting systems*, Energy Environ. Sci. **5**, 9922 (2012).

[52] M. Suermann, K. Takanohashi, A. Lamibrac, T. J. Schmidt, and F. N. Büchi, *Influence of operating conditions and material properties on the mass transport losses of polymer electrolyte water electrolysis*, J. Electrochem. Soc. **164**, F973 (2017).

[53] A. P. Thompson, H. M. Aktulga, R. Berger, D. S. Bolintineanu, W. M. Brown, P. S. Crozier, P. J. in 't Veld, A. Kohlmeyer, S. G. Moore, T. D. Nguyen, R. Shan, M. J. Stevens, J. Tranchida, C. Trott, and S. J. Plimpton, *LAMMPS—A flexible simulation tool for particle-based materials modeling at the atomic, meso, and continuum scales*, Comput. Phys. Commun. **271**, 108171 (2022).

[54] L. Martínez, R. Andrade, E. G. Birgin, and J. M. Martínez, *PACKMOL: A package for building initial configurations for molecular dynamics simulations*, J. Comput. Chem. **30**, 2157 (2009).

[55] J. L. F. Abascal and C. Vega, *A general purpose model for the condensed phases of water: TIP4P/2005*, J. Chem. Phys. **123**, 234505 (2005).

[56] P. Habibi, A. Rahbari, S. Blazquez, C. Vega, P. Dey, T. J. H. Vlugt, and O. A. Moultos, *A new force field for* OH^- *for computing thermodynamic and transport properties of* H_2 *and* O_2 *in aqueous NaOH and KOH solutions*, J. Phys. Chem. B **126**, 9376 (2022).

[57] J.-P. Ryckaert, G. Ciccotti, and H. J. C. Berendsen, *Numerical integration of the Cartesian equations of motion of a system with constraints: Molecular dynamics of n-alkanes*, J. Comput. Phys. **23**, 327 (1977).

[58] R. Hockney and J. Eastwood, *Computer Simulation Using Particles* (CRC Press, Boca Raton, USA, 1988).

[59] S. Nosé, *A unified formulation of the constant temperature molecular dynamics methods*, J. Chem. Phys. **81**, 511 (1984).

[60] W. G. Hoover, *Canonical dynamics: Equilibrium phase-space distributions*, Phys. Rev. A **31**, 1695 (1985).

[61] W. G. Hoover, *Constant-pressure equations of motion*, Phys. Rev. A **34**, 2499 (1986).

[62] I.-C. Yeh and G. Hummer, *System-size dependence of diffusion coefficients and viscosities from molecular dynamics simulations with periodic boundary conditions*, J. Phys. Chem. B **108**, 15873 (2004).

[63] S. H. Jamali, A. Bardow, T. J. H. Vlugt, and O. A. Moultos, *Generalized form for finite-size corrections in mutual diffusion coefficients of multicomponent mixtures obtained from equilibrium molecular dynamics simulation*, J. Chem. Theory Comput. **16**, 3799 (2020).

[64] A. S. Emam, M. O. Hamdan, B. A. Abu-Nabah, and E. Elnajjar, *Enhancing alkaline water electrolysis through innovative approaches and parametric study*, Int. J. Hydrog. Energy **55**, 1161 (2024).

[65] R. J. Gilliam, J. Graydon, D. Kirk, and S. Thorpe, *A review of specific conductivities of potassium hydroxide solutions for various concentrations and temperatures*, Int. J. Hydrog. Energy **32**, 359 (2007).

[66] B. Ross, K. Skidmore, S. Haussener, and K. Brinkert, *Transient simulation of gas bubble evolution and overpotential dynamics for the hydrogen evolution reaction*, ACS Electrochem. **2**, 113 (2025).